remote sensing

MDPI

Article

Coastal Subsidence Monitoring Associated with Land Reclamation Using the Point Target Based SBAS-InSAR Method: A Case Study of Shenzhen, China

Bing Xu [1], Guangcai Feng [1,*], Zhiwei Li [1], Qijie Wang [1], Changcheng Wang [1] and Rongan Xie [2]

[1] School of Geosciences and Info-Physics, Central South University, Changsha 410083, China; xubing@csu.edu.cn (B.X.); zwli@csu.edu.cn (Z.L.); qjwang@csu.edu.cn (Q.W.); wangchangcheng@csu.edu.cn (C.W.)

[2] Guangdong Institute of Surveying and Mapping of Geology, Guangzhou 510800, China; 13902396961@139.com

* Correspondence: fredgps@gmail.com; Tel.: +86-731-888-30573

Academic Editors: Zhenhong Li, Roberto Tomas, Zhong Lu and Prasad S. Thenkabail
Received: 30 May 2016; Accepted: 5 August 2016; Published: 13 August 2016

Abstract: Shenzhen, the first special economic zone of China, has witnessed earth-shaking changes since the late 1980s. In the past 35 years, about 80 km^2 of land has been reclaimed from the sea in Shenzhen. In order to investigate coastal vertical land motions associated with land reclamation, we proposed an elaborated Point Target (PT) based Small Baseline Subset InSAR (SBAS-InSAR) strategy to process an ENVISAT ASAR ascending and descending orbits dataset both acquired from 2007 to 2010. This new strategy can not only select high density PTs but also generate a reliable InSAR measurement with full spatial resolution. The inter-comparison between InSAR-derived deformation velocities from different orbits shows a good self-consistency of the results extracted by the elaborated PT-based SBAS-InSAR strategy. The InSAR measurements show that the reclaimed land is undergoing remarkable coastal subsidence (up to 25 mm/year), especially at the Shenzhen Airport, Bao'an Center, Qianhai Bay and Shenzhen Bay. By analyzing the results together with land reclamation evolution, we conclude that the ground deformation is expected to continue in the near future, which will amplify the regional sea level rise.

Keywords: coastal subsidence; land reclamation; PT-based SBAS-InSAR; sea level rise; Shenzhen

1. Introduction

The Coastal Zone [1] plays a very important role in transportation, the circulation of resources and funds, etc. To promote urbanization and economic development, land reclamation [2] from the sea is a common practice for many countries in the world, such as USA [3], Japan [4], Italy [5], the Netherlands [6,7], and China [8–10].

Over the past decades, Synthetic Aperture Radar Interferometry (InSAR) [11,12] has been proven to be a powerful geodetic technique, and been extensively exploited to investigate ground deformation induced, for example, by earthquake [13–15] or volcano activities [16,17]. Furthermore, recently remarkable improvements in Multi-Temporal InSAR (MT-InSAR), including the Small Baseline Subset InSAR (SBAS-InSAR) [18,19] and the Persistent Scatterer InSAR (PS-InSAR) [20–23], enable us to monitor long period surface deformation caused by permafrost [24], ground water extraction [25–28], mining [29], and land reclamation [30]. The MT-InSAR exploits a set of high phase-quality pixels [20], other than the original full two-dimensional image grid, to map the deformation history and the corresponding average deformation velocity. It can overcome most intrinsic temporal and geometric

decorrelations [25] of conventional InSAR, and simultaneously estimate the atmospheric effect [26–29] to generate high accuracy deformation results. In recent years, researches that investigated the ground deformation related to land reclamation by MT-InSAR have been carried out in reclaimed lands around the world, such as the Chek Lap Kok Airport in Hong Kong [30], Sibari in Southern Italy [31], and the Venice coastland [32]. Besides the MT-InSAR techniques, geodetic techniques [33], such as GPS and leveling, have been widely used in ground deformation monitoring. However, the MT-InSAR could provide a better spatial resolution to capture the deformation details compared with GPS or leveling.

Shenzhen is a city built on the weak alluvial clay [34] of sludge and reclaimed land. Due to high compressibility, low permeability, and weak strength of the alluvial clay [35], the soil becomes compacted under the pressure from constructions and clay self-consolidation. The compaction process causes ground deformation [36], threatening the stability of ground constructions and underground man-made facilities [37]. Therefore, ground deformation monitoring is very important for the reclaimed land utilization in Shenzhen. Dense Point Targets (PTs) for deformation monitoring can be selected from built-up area [20] that maintains long-time high coherence, while for the non-built-up area, e.g., reclaimed land, for the area surrounding buildings built on the reclaimed land, few PTs can be selected [38]. Although previous studies [36,39] have tried to capture the deformation in urban areas with MT-InSAR, the following two issues remain unsolved: (1) When traditional MT-InSAR methods are used, the ground deformation is not well determined due to the low PTs density in the reclaimed land; (2) The deformation associated with land reclamation has not yet been analyzed. So how to select the appropriate number of usable PTs for MT-InSAR deformation monitoring and the analysis of the deformation results needs to be further studied for the reclaimed land of Shenzhen.

In this study, an elaborated PT-based SBAS-InSAR strategy is proposed to select usable PTs and generate an InSAR measurement with full spatial resolution. Based on the selection of PTs, two independent ENVISAT ASAR datasets along the ascending and descending orbits were used to map the coastal land deformation in Shenzhen between 2007 and 2010. Inter-comparison of the InSAR measurements from different orbits was carried out to check the self-consistency of the measurements. Finally, we discussed the implications and potential subsidence hazards caused by land reclamation in this area.

2. Background of Study Area

2.1. Geological Environment

Shenzhen is located at the southeast of the Pearl River Delta (PRD) region in China. The city has complicated topography and is surrounded by the sea in the south and the west. Its elevation ranges between 1 and 10 m in the southwest of Shenzhen, reaches 30 m in the heart of the city, and goes up to 80 m at the northeast (see Figure 1). The marine sediments of the Quaternary period widely spread across the low-lying coastal land areas. This sediment layer is of high water content and high compressibility, big void ratio, and weak shearing strength [35]. The thickness of this layer is generally 3–10 m, but is up to 20 m in some particular areas [40].

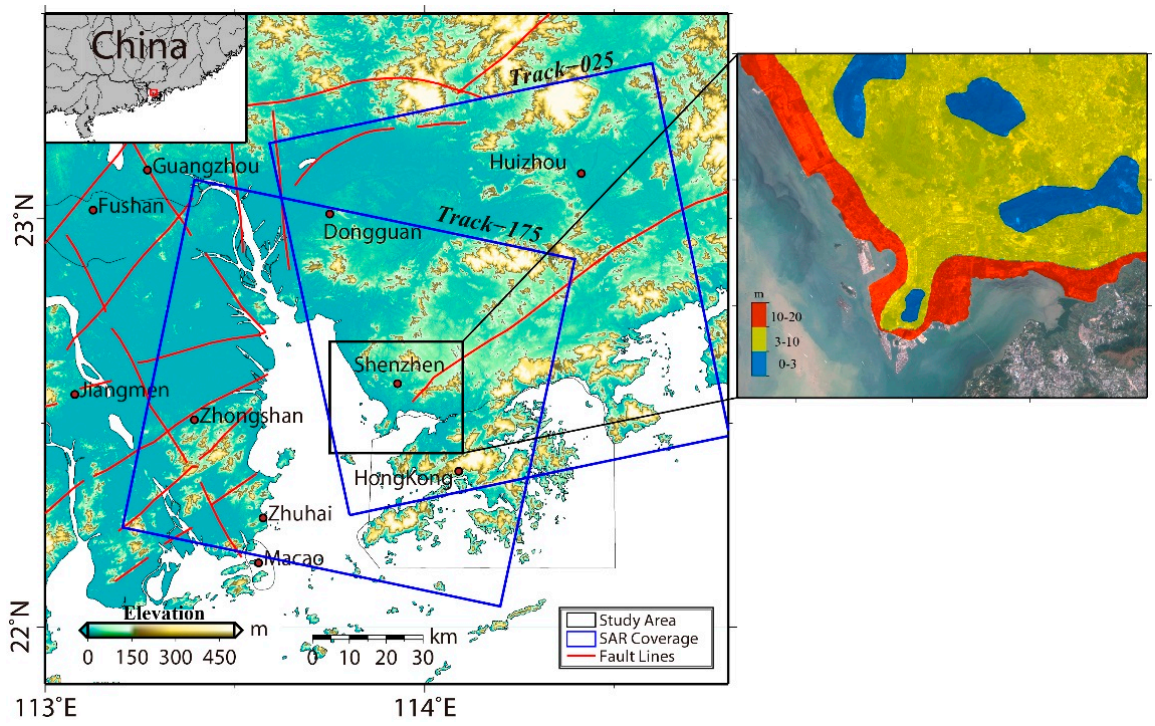

Figure 1. Study area and SAR data coverage. The study area is outlined by the black rectangle. Blue rectangles represent the coverage of the SAR dataset used. Red lines denote the fault lines surrounding [41,42]. Inset, the approximate location of Shenzhen in China. The right sub-figure is the distribution of the sediment layer in Shenzhen. The colors indicate the thickness.

2.2. Historical Land Reclamation

Due to its geographical location, Shenzhen is the direct link between the China mainland and Hong Kong. With its economic development and boom [43], the demand for land use [44] is increasing. The comparison of Landsat satellite images (see Figure A1) shows the dramatic landscape changes in Shenzhen from 1979 to 2015. Small hills were leveled, and thousands of high buildings have replaced previous agricultural and vegetated areas. Meanwhile, 80 km^2 of land has been reclaimed from the sea along the coastal zone in the past 35 years [45]. The temporal and spatial evolution of land reclamation [43] is shown in Figure 2. Land reclamation has brought considerable economic benefits [46] to the government and led to further economic development in Shenzhen. However, long-time compaction of the reclaimed land causes ground deformation [30], which affects the stability of the surface and underground constructions, thereby threatens the safety of people's lives and assets.

According to an investigation conducted by the Geological Bureau of Shenzhen, Shenzhen is in a stable tectonic environment with low tectonic hazard risk [41]. However, local ground deformation [1,42] related to anthropogenic activity has become the major geohazard in Shenzhen, especially in the coastal reclaimed areas.

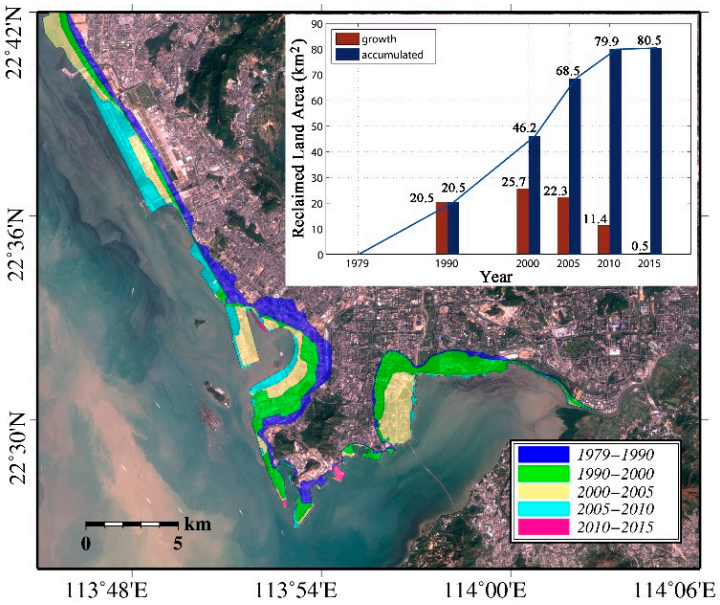

Figure 2. Land reclamation and its evolution in Shenzhen. The reclaimed land for every period is spatially overlapped on the Landsat-8 background. Inset shows the temporal evolution. The coastlines are extracted from a set of co-registered Landsat images shown in Figure A1. Firstly, coastlines are automatically extracted by image segmentation with an appropriate threshold. Then the initial coastlines are overlaid to the Landsat image in ArcGIS software—we edited the inaccurate coastline manually.

3. Dataset and Methodology

3.1. Dataset

Two sets of ENVISAT ASAR data acquired between 2007 and 2010, along the ascending (31 scenes, see Table A1 for detail) and descending orbits (28 scenes, see Table A2 for detail), were employed to analyze the coastal deformation. Two dense networks of SBAS interferometric pairs (see Figure 3) with both short perpendicular and temporal baselines were used in the data processing. The available multi-orbit datasets allow us to validate the self-consistency of the monitoring results by inter-comparison.

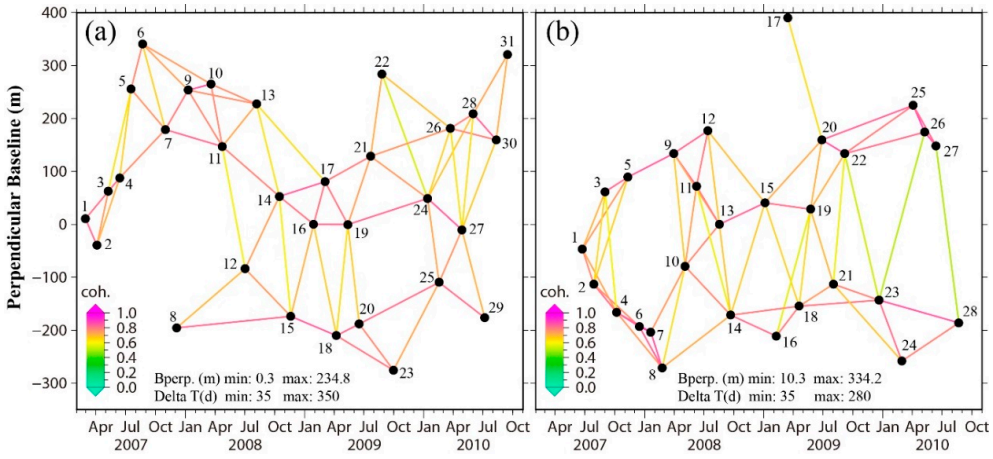

Figure 3. SBAS networks of the datasets used. (**a**) Track 025; (**b**) track 175. Each black dot denotes one image. The line between each two dots represents one interferometric pair, whose color indicates the average coherence of the corresponding interferogram.

3.2. PT-Based SBAS-InSAR Strategy

In our study area, due to the vegetation covering and humid subtropical climate, the application of SAR interferometry is mainly limited by temporal decorrelation [25,47] and inhomogeneity in the tropospheric path delay [27,28]. Besides, the land reclamation related deformation has limited spatial range, thus we do not multi-look the interferograms to retain deformation details. We processed the datasets with an elaborated PT-based SBAS-InSAR, and below (Figure 4) is a flow chart showing the strategy, which consists of four major processing steps.

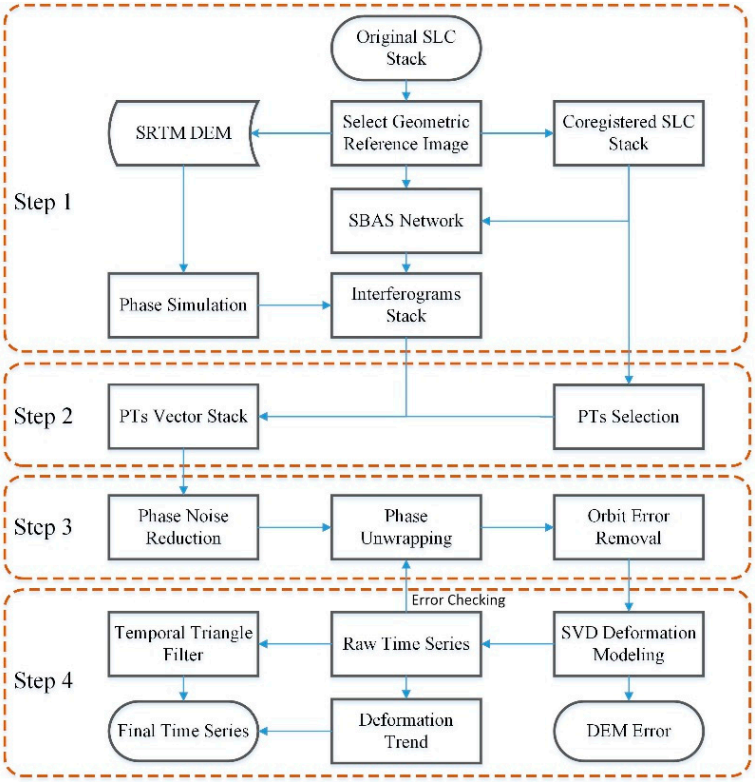

Figure 4. Flow chart of the elaborated PT-based SBAS-InSAR.

3.2.1. Pre-Processing

Data processing starts with a stack of Single Look Complex (SLC) images [48]. To minimize the effect of mis-coregistration caused by geometric, temporal, and Doppler decorrelations [25], the images acquired on 28 January 2009 and 17 August 2008 for track 025 and track 175, respectively, were chosen as geometry references for SLC coregistration using the Formula (4.1) of reference [49]. Interferometric pairs with both short perpendicular and temporal baselines were selected to construct networks of the SBAS interferometric pairs. Also, two dense networks of SBAS interferometric pairs (for details see Table 1 and Figure 3) were established. The topographic phase in each interferogram was removed with the 3-arc SRTM DEM [50]. To preserve the detail deformation pattern, the multi-looking process was not applied to any interferogram pairs. A reference point, black star in Figures 5 and 6, was chosen from an inland low-rise building in a stable area.

Table 1. Summary information of the networks of SBAS interferometric pairs.

Orbit Type	Track	No. of SLC Images	No. of Pairs	Temporal Span
Ascending	025	31	69	28 February 2007–15 September 2010
Descending	175	28	65	24 June 2007–22 August 2010

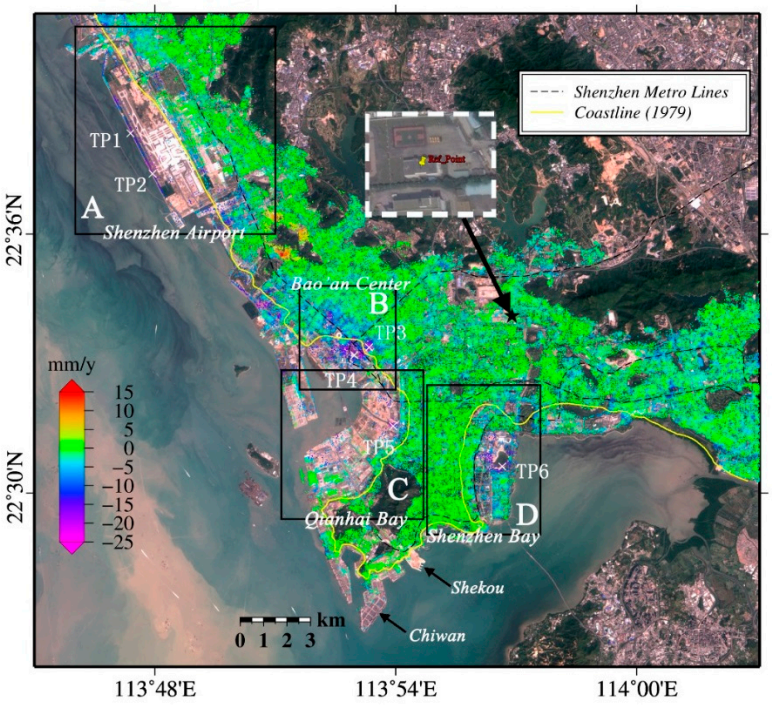

Figure 5. Deformation rates generated with track 025 dataset for the whole study area. The black star locates the reference point, and the inset shows a more detail location of it. Black dashed lines represent the Shenzhen Metro Lines. The yellow line denotes the coastline in 1979. The background is a Landsat-8 image acquired in 2015. Regions A, B, C, and D marked with black rectangles will be further analyzed together with land reclamation in the discussion section. Points marked with white cross (×) are selected to show time series deformation.

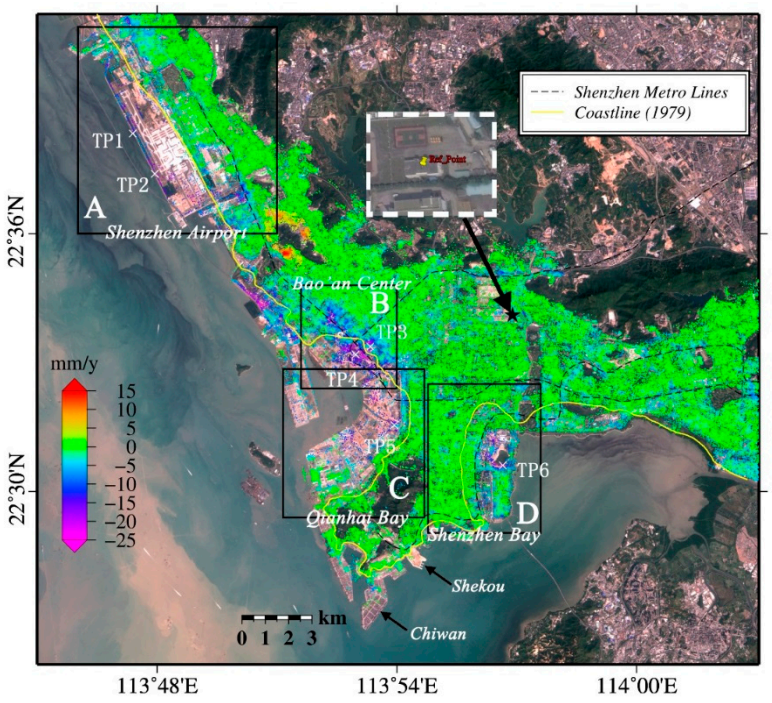

Figure 6. Deformation rates generated with track 175 dataset for the whole study area. Other remakes are the same as those in Figure 5.

3.2.2. Improved Point Target Selection

Recently, many researches demonstrated that exploiting point-like scatterers [20,21] instead of a two-dimensional grid for deformation monitoring can overcome the effect of interferometric decorrelation [25,51]. The selection of more usable PTs in a low-coherence area [21] for deformation retrieval is a key issue in MT-InSAR data processing. In our study, the coastal reclaimed land may undergo significant deformation and the backscattering coefficients may vary significantly in the time domain. As a consequence, these two factors limit the application of the dispersion of amplitude (DA) method [20] or the distributed scatterers (DS) method [38] to select sufficient usable PTs. Besides, as a phase quality indicator, the coherence maps associated with the interferometric phase could be exploited to identify usable targets. Point target with coherence greater than a given threshold could be selected as a usable PT. However, the coherence is underestimated, as the phase values are non-stationary. Thus non-stationary signals, including DEM, atmospheric effect [26] and possibly the target motion should be estimated and thus be removed. The space averaging of the data inside a certain window (e.g., 50 m $\times$ 50 m) is used as the estimation of these non-stationary signals [21] for the center pixel of the window. However, this is not a common case because the average value may not be the genuine estimate [51].

To select adequate usable PTs, an elaborated strategy based on Spectral Diversity of SLC images [48] and the SBAS network [18] is exploited. The concept of spectral diversity originates from Interferometric Point Target Analysis (IPTA) [52], whose principle is that the energy of usable PTs remains almost the same when processing different looks with fractional azimuth and different range bandwidths. We calculated the spectral diversity map γ for each co-registered SLC image, and selected a point target as a usable PT, which has the weighted average of the time series spectral diversity values greater than a given threshold (e.g., $\overline{\gamma} > 0.38$). Given M SLC images, and N interferometric pairs in the SBAS network, then $\overline{\gamma}$ can be expressed as

$$\overline{\gamma}(r,a) = \frac{1}{2N}\sum_{m=1}^{M} n_m \cdot \gamma_m(r,a) \tag{1}$$

where $\gamma_m(r,a)$ is the spectral diversity value at pixel location (r, a) (range, azimuth) for the m-th SLC image, n_m denotes the frequency of the m-th SLC image used in the SBAS network, and

$$2N = \sum_{m=1}^{M} n_m \tag{2}$$

Our PT selection strategy is consistent with the one based on the mean interferometric coherence of interferogram stack for SBAS-InSAR. In the coherence-based method, the more frequently a SLC image is used to combine an interferometric pair, the larger the weight factor would be assigned to this image in calculating the mean interferometric coherence for the SBAS network interferogram stack. Similarly, using the frequency of a SLC image as the weight factor in the calculation of mean spectral diversity map $\overline{\gamma}$, would also adjust the influence of that image's spectral diversity map accordingly. The spectral diversity map could be treated as the Signal-to-Noise Ratio (SNR) indicator of the SLC pixel's phase. Two pixels with high spectral diversity values would generate high quality interferometric phases, and vice versa. As a consequence, the weighted spectral diversity map $\overline{\gamma}$ is the equivalence of the SNR of the interferometric phases for the given SBAS network, which allows a more accurate PT selection in SBAS-InSAR.

After the PT selection, the data information, including the interferometric phases, spatial coherence etc., is extracted from the two-dimensional grid and stored in vector format for subsequent data processing.

3.2.3. Phase Filtering, Orbital Phase Error Removal and Phase Unwrapping

In order to reduce the phase noise, the differential interferometric phase for PTs, was spatially filtered by an improved SUSAN filter [53,54] with a search window size of 11 $\times$ 11 (range $\times$ azimuth)

pixels. This method can avoid noise contamination from unusable PTs. The spatial coherence for each PT was estimated with the same window. Subsequently, the smoothed phase of each interferometric pair from the SBAS network was unwrapped by the method based on network programming [55] with the spatial coherence as the weight factor.

In InSAR processing, the flat-earth phase component is removed with precise orbits. For ENVISAT, it has an accuracy of 5–7 cm radially and 10–15 cm cross-track [56], and its residual orbital phase error [57] with long wavelength character may remain in the interferogram. Such error is easy to discriminate from the local deformation in our study area. Hence, we estimated the orbital error using quadratic polynomial models [57] and removed it the error from the unwrapped interferogram. It needs to be noted that the quadratic models would also absorb long-wavelength components of atmospheric effect [27,28].

3.2.4. Modeling of Deformation and Unwrapping Error Checking

The Singular Value Decomposition (SVD) method was employed to solve the rank-deficient problem [18] in SBAS-InSAR deformation modeling. The raw time series deformations that are contaminated by atmospheric delay and phase noise and DEM error correction can be obtained based on the unwrapped phase obtained in Section 3.2.2. The reliability of phase unwrapping was evaluated via the phase difference between the unwrapped phase and the one simulated with raw time series deformation, especially for Qianhai Bay and Shenzhen Bay where sparsely distributed PTs are identified. If the interferometric phase was unwrapped with error, then the phase difference would be significantly large. We then computed the histograms of phase difference for statistics (see Tables A3 and A4). We can see that over 82% of PTs were unwrapped with an error less than 0.5 rad for Qianhai Bay, and 83.3% and 86.4% of the PTs were unwrapped for track 025 and track 175. For these two areas, over 95% of the PTs were unwrapped with error less than 1.0 rad. Additionally, the result showed that over 95% of PTs were unwrapped with error less than 1.0 rad for the whole study area. As a result, we believe that the interferometric phase was unwrapped without significant error.

In order to remove the error of atmospheric delay and phase noise from the raw time series deformations, the linear regression with the raw time series deformations was firstly carried out to inverse the mean deformation velocity map [18]. Then the inverted linear deformation was subsequently subtracted from the raw time series deformations calculated previously. The remaining components are the non-linear ground deformation, atmospheric delay, and random phase noise. Non-linear ground deformations might have some degree of correlation (low-pass) in the temporal domain, while atmospheric delay and phase noise are both high-pass, thus non-linear deformation can be separated by the temporal triangle weighted low-pass filter [20] with a certain length of time window (e.g., 180 days). Finally, we obtained the total deformation by adding up the linear deformation and non-linear deformation.

4. Results

Due to the side-looking geometry, the InSAR measurement is the sum of the projections of ground three-dimensional (3-D) ground deformations in the (Line-of-Sight) LOS direction. In Shenzhen coastal zone, the subsidence of the reclaimed land and sediment layer dominates the ground deformation. Hence, the deformation in our study area was assumed mainly in the vertical direction and the LOS displacement was directly back-projected into the vertical direction using the local incidence angle [36].

4.1. Deformation Rate Maps

The deformation rate maps generated from the ascending and the descending data are between –25 mm/year and 15 mm/year, as shown in Figures 5 and 6, respectively. The deformation patterns are very similar, suggesting that vertical subsidence dominates the coastal deformation. The deformation rate maps demonstrate that most of the inland area within the coastline in 1979 is stable, which means the selected reference point did not undergo obvious deformation. However, the reclaimed land area

along the coastline in 1979 (the yellow line in Figures 5 and 6) experienced significant subsidence, especially at Shenzhen Airport, Bao'an Center, Qianhai Bay, and Shenzhen Bay, marked by black rectangles in Figures 5 and 6. Obvious deformation was not observed in the Chiwan and Shekou harbors, because the foundation of the wharf apron space was enhanced by using special rammer of small base [35]. Besides, we also observed non-uniform deformation in the mean deformation rate maps. The phenomenon is particularly evident in the developed urban region B, Bao'an Center, where many roads and high rise buildings cover the reclaimed land. In addition to the ground subsidence, there are several patches with remarkable uplift located around the right bottom corner in region A. The positive deformation signal may be related to the rise of groundwater level [46]. This area is an old industrial district, where a great amount of groundwater was extracted for production. Now the factories are moving out, decreasing the groundwater extraction [46]. As a result, the groundwater level is recovering.

To validate the non-uniform subsidence, field work was carried out at Bao'an Center (around point TP4) in 2011. Figure 7a,b show remarkable effects of the differential subsidence rates observed at a road and a building. This is because they were built on different foundations. The black arrows in Figure 7 point to the side with solid foundations, which may have slight subsidence. While, red arrows point to the side with unreinforced foundations, where remarkable subsidence occurred.

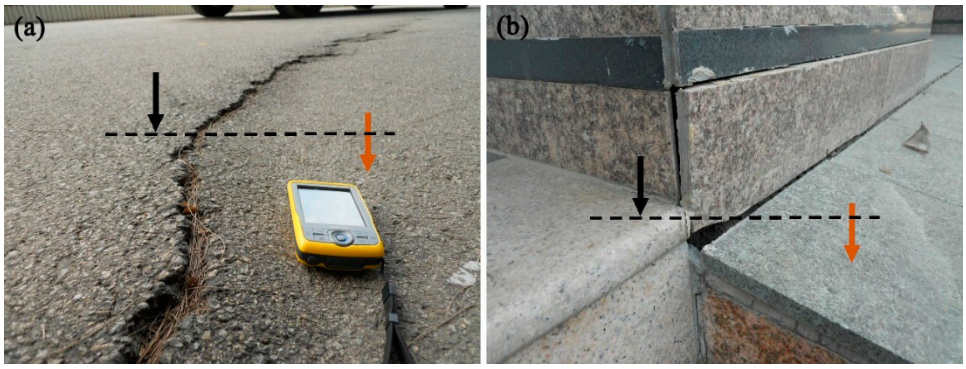

Figure 7. Field work pictures showing non-uniform subsidence. (**a**) Site of a road; (**b**) site of a building.

4.2. Time Series of Selected Points

Several points were selected to show the time series deformation (see Figure 8). The image dataset start time is usually taken as the reference time of the time series in the SBAS-InSAR technique. As seen in Table 1, the two datasets have different start times. For comparison, we set one reference time for these two datasets as 28 February 2007. As a consequence, the time series deformations mapped in the descending orbit was shifted with a constant, which was calculated according to the deformation rate and time difference (116 days). Clearly, in the reclaimed land, TP1, TP2, TP4, PT5, and TP6, are subsiding linearly (see Figure 8). TP3, located inland according to the coastline in 1979, has a different temporal pattern, showing that the TP3 was in rapid deformation (−31.7 mm/year) before January 2009, then its deformation was slowed down (−18.6 mm/year) between January 2009 and January 2010, and finally the area became stable. This deformation is very consistent with the pattern from predictions of the consolidation theory of unsaturated soil [58]. Although the subsidence rate at each selected point is slightly different, the time series obtained from the ascending and descending orbits matched well.

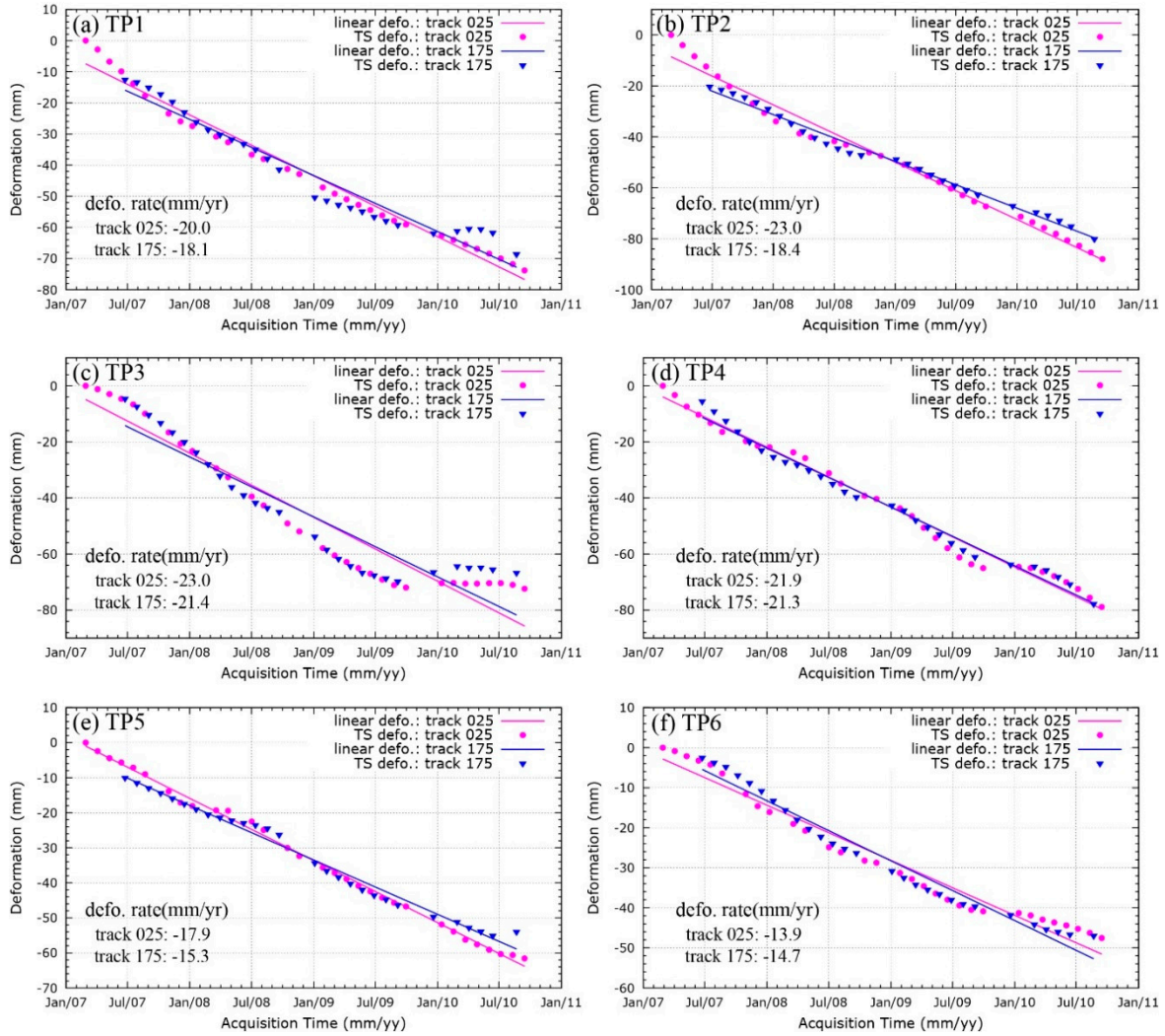

Figure 8. Time series of the deformation at selected points. (**a**) TP1; (**b**) TP2; (**c**) TP3; (**d**) TP4; (**e**) TP5; (**f**) TP6. Purple dots and blue triangles represent the ascending (025) and descending (175) tracks. Purple lines and blue lines represent the linear deformations. The corresponding slopes are given in the lower left corner.

5. Discussion

5.1. Self-Consistency Checking by Inter-Comparison between the Ascending and Descending InSAR Measurements

In order to quantitatively check the self-consistency of InSAR measurements, inter-comparison of the deformation rates between ascending and descending results was carried out. Due to the uncertainty in SAR geo-location [59], the PTs from different orbits were unlikely to be at the exact same locations. The resolution of the results is down-sampled to reduce the effect of the geo-location uncertainty [60]. Firstly, a data grid with a resolution of 50 m $\times$ 50 m was created with the tradeoff between the deformation detail and resolutions. Then InSAR measurements from the ascending and descending orbits were resampled respectively to the defined data grid by Pixel Aggregate [61]. Finally, the InSAR measurements from different orbits were compared. We assumed that the InSAR measurements on the defined grid had a common deformation signal. The inter-comparison results between the ascending and descending InSAR-derived deformation rates showed that correlation between the two InSAR measurements is 0.92, revealing that the InSAR measurements mapped by

our PT-based SBAS-InSAR strategy are in good agreement with each other. The Root-Mean-Square Error (RMSE) of the difference between the ascending and descending orbits is 1.8 mm/year, implying that the InSAR measurements are highly self-consistent. However, there are points lying away from the fitted model (the purple line in Figure 9), which may be caused by the errors in InSAR measurements [57], errors in SAR geo-location [59] (mismatch of the measurements from different viewing geometries), horizontal displacement and possibly the non-linear deformation process [20].

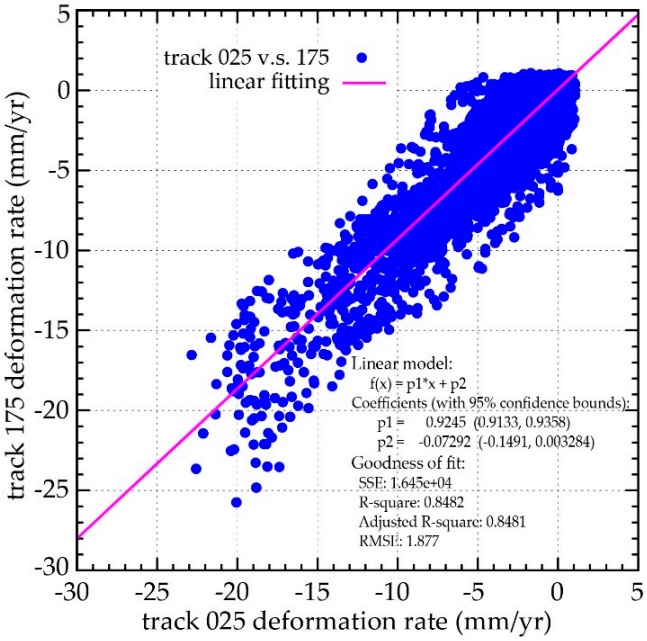

Figure 9. Inter-comparison of the deformation rates between track 025 and track 175. Blue dots denote the measured points on track 025 and track 175. The purple line is the fitted linear model, i.e., f(x) = 0.9245x − 0.07292.

5.2. Deformation Associated with Land Reclamation

As the first special economic zone of China, Shenzhen has witnessed great changes since the 1980s, accompanied by extensive land reclamation over the past 30 years. The InSAR measurements of regions A, B, C, and D (Figures 5 and 6) are zoomed in Figures 10–13. According to the InSAR measurements, we can observe remarkable deformation in most of the reclaimed land, and the maximum rate is up to 25 mm/year. Generally, ground deformation is induced by primary compaction and secondary compression of the alluvial clay beneath the reclamation [30]. Previous investigations [30,58] showed that 90% primary compaction of alluvial clay in Hong Kong Chek Lap Kok Airport, a site that has very similar land reclamation activity to our study area, took about 10 to 20 years, and longer for a thickness sediment layer. As shown in Figure 2, about 34.3 km^2 of land, accounting for 42.6% of the total, was reclaimed from the sea during the past 15 years (period of 2000–2015), on which large infrastructure has been built. Thus, ground settlement is expected in most of the reclaimed area.

Figure 10 shows different subsidence patterns for the new airport built on reclaimed land and the old airport built inland. The new airport was built between years 2000 and 2010 (See Figure 11), thus few PTs were selected from that region. Numerous PTs were identified along the dam to the west part of the new airport. Although the new airport was reclaimed gradually (see the coastline change in Figure 10, the yellow line, yellow dash line, magenta dash line, and the white dash line), remarkable deformation was observed during different phases. For region B (Figure 11), Bao'an center, where many high-rise buildings stand, remarkable subsidence signals in the reclaimed land and along the Metro Lines were detected in both ascending and descending datasets (Figure 11). The Bao'an Center was mainly reclaimed in the period 1979–1990 (the area along the coastlines between 1979 and 1990,

see Figure 11). However, it still undergoes remarkable ground deformation, which may be induced by engineering construction. Slight subsidence was observed on the newly reclaimed land (the area outside the coastline of 1990), as little urban construction is in progress. If a new construction were to be built, the temporary equilibrium could be broken, which may cause additional ground deformation. The Qianhai Bay, an unexploited reclaimed land area, has a few sites with high deformation rates (see Figure 12) caused by compaction of the reclaimed foundation and the alluvial soil beneath. The detail subsidence rate maps of Shenzhen Bay are shown in Figure 13. The results revealed that the body of Shenzhen Bay Check Point is in a weak deformation state ($[-6, -3]$ mm/year), while evident settlements were observed in some sites of the reclaimed land, especially the north part of the Check Point. High deformation rates were also detected along the Shenzhen Metro Line (black dash line in Figure 13), which was centered on the reclaimed land. Based on these, we can conclude that remarkable subsidence has occurred on the lands reclaimed 15 years before, such as the Bao'an Center.

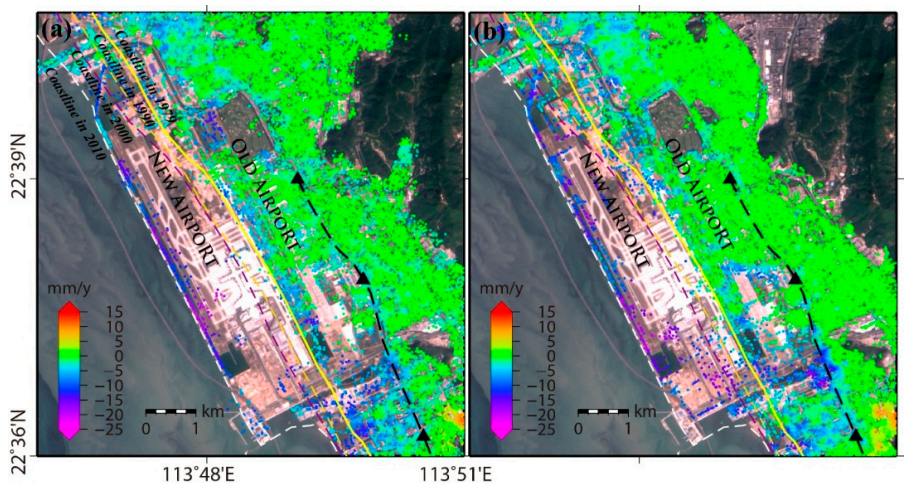

Figure 10. Subsidence rate of Region A of Figures 5 and 6, Shenzhen Airport. (**a**) Track 025; (**b**) track 175. Black dash line with black triangles represents the Shenzhen Metro Line, and the black triangle denotes the Metro station. The yellow line denotes the coastline in 1979. Background is a Landsat-8 image acquired in 2015.

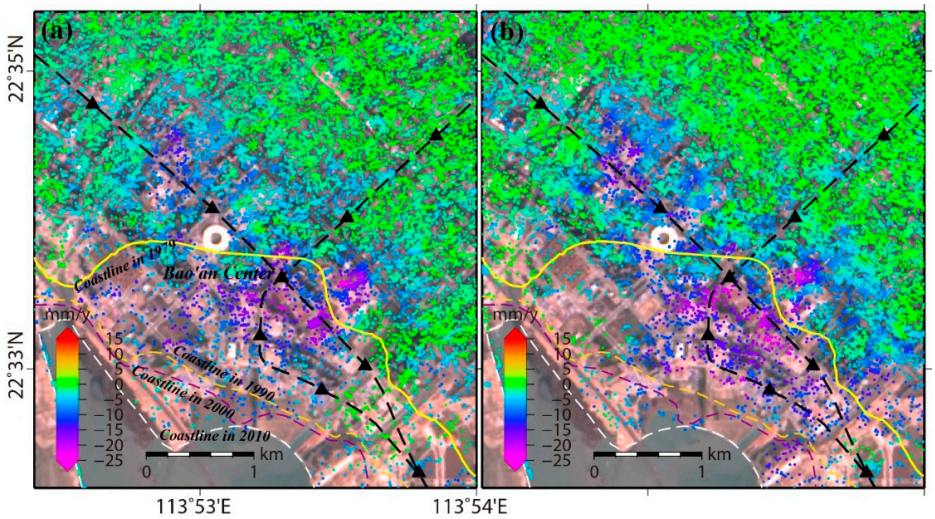

Figure 11. Subsidence rate of Region B of Figures 5 and 6, Bao'an center. (**a**) Track 025; (**b**) track 175. Other remakes are the same as in Figure 10.

In addition, the engineering constructions, e.g., the construction of Shenzhen Airport and urbanization of Bao'an, would also contribute to subsidence. Considering the deformation maps and time series at selected points, we believe that the four major land reclamation regions are undergoing remarkable subsidence, which can be expected to continue in the near future. Work to further monitor the ground subsidence shall focus on the coastal land reclamation region, especially Shenzhen Airport, Bao'an Center, Qianhai Bay, and Shenzhen Bay.

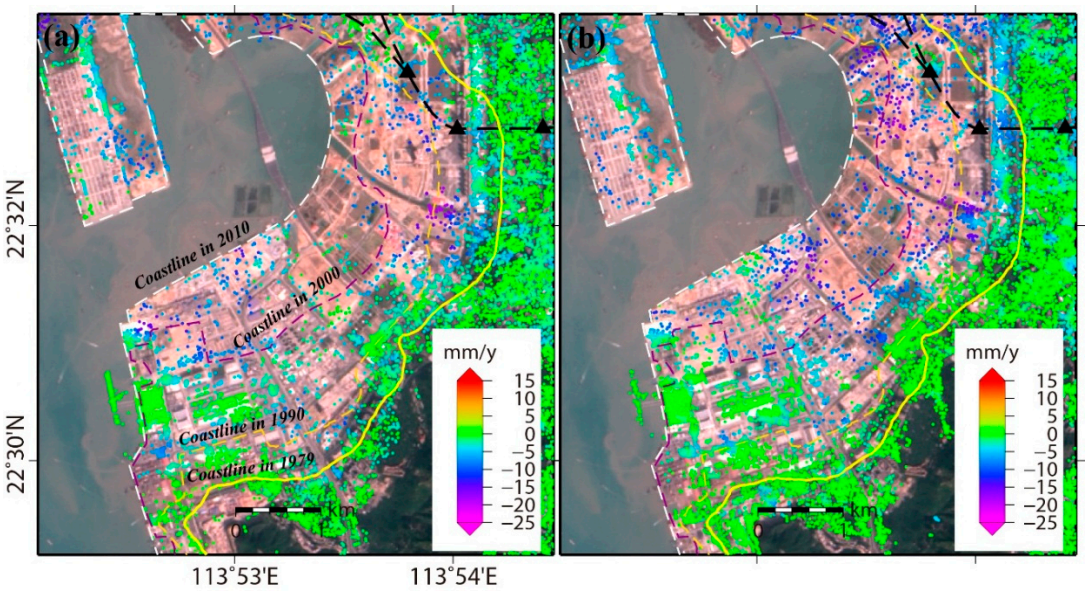

Figure 12. Subsidence rate of Region C of Figures 5 and 6, Qianhai Bay. (**a**) Track 025; (**b**) track 175. Other remakes are the same as in Figure 10.

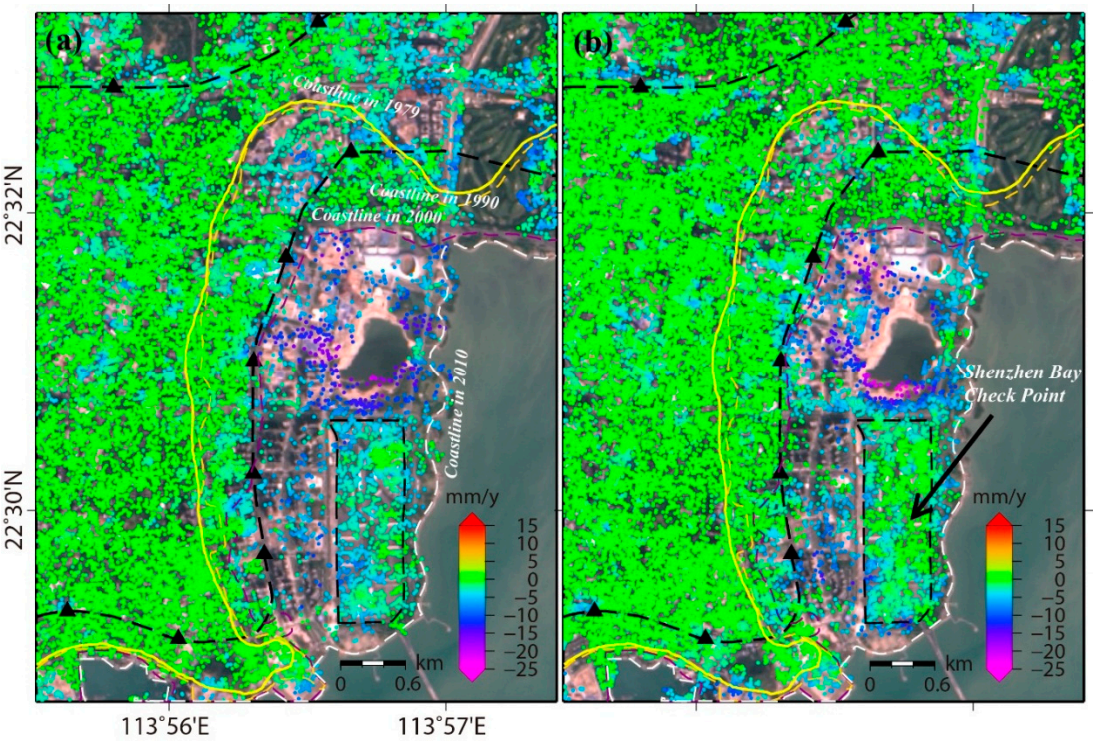

Figure 13. Subsidence rate of Region D of Figures 5 and 6, Shenzhen Bay. (**a**) Track 025; (**b**) track 175. Other remakes are the same as in Figure 10.

5.3. Effects of Coastal Subsidence Coupled with Sea Level Changes

The subsidence of the reclaimed land threatens infrastructure, and contributes to the relative sea level changes [62], which may cause saltwater intrusion [63,64] and destroy coastal biodiversity [37]. Assuming a mean sea level rise of 2.5 mm/year [33,65], the selected regions A, B, C, and D (shown in Figures 10–13) would fall to sea level in 114, 121, 225, and 313 years (see Table 2). Compared with previous studies [38], our deformation rate is slightly larger due to the fact that more PTs have been selected from significant deformation areas in our method. As a consequence, the large deformation rate areas have no measurement of their results whereas appropriate PTs have been identified by our method for deformation mapping. So the difference between their results and ours is expected. The risk assessment based only on sea level rise had been underestimated in the Shenzhen coastal zone because of the amplification effect from coastal subsidence. To decelerate the relative sea level rise, effective measures, such as reinforcing the ground foundation, need to be taken to prevent subsidence in the coastal zone [66].

Table 2. Estimation of the elapsed time of land surface falling sea level regarding coastal subsidence in selected regions.

Region	Elevation [1] H (m)	Sea Level Rise v_1 (mm/year)	Subsidence Rate[2] v_2 (mm/year)	Elapsed Time [3] Estimated T (year)
Shenzhen Airport	1.5	2.5	−10.7	114
Bao'an Center	1.8	2.5	−12.4	121
Qianhai Bay	1.8	2.5	−5.5	225
Shenzhen Bay	2.0	2.5	−3.9	313

[1] average elevation of region; [2] average subsidence rate of region; [3] $T = H \times 1000/(v_1 - v_2)$.

5.4. Potential and Limits of InSAR in Mapping Coastal Subsidence

The InSAR measurements from both ascending (track 025) and descending (track 175) orbits showed a very similar pattern in the deformation rate maps (Figures 5, 6 and 10–13) derived by PT-based SBAS-InSAR, and the displacement time-series of the selected points (Figure 8). In order to properly map the coastal deformation associated with land reclamation, the effect of low-coherence will be considered in the implementation of data processing. To illustrate this problem, the dataset from track 175 was also processed with the STAMPS PS method. The comparison (see Appendix B for detail) between STAMPS result and ours showed that few PTs (see Figures B1–B3) have been selected by STAMPS due to long time decorrelation. Although the two results (see Figures B2 and B3) have a similar deformation trend in slight deformation areas, our method has much denser measurements in both significant deformation and stable urban areas, because the PT-based SBAS-InSAR method utilizes multi-reference to overcome the decorrelation effect of single reference interferometric phases, whereas the STAMPS could only select coherent PTs over a long time. As a consequence, such difference is expected. The results show that our method has great potential in mapping coastal deformation. However, our PT-based SBAS-InSAR technique also has its limitations. First, the threshold for PT selection needs to be carefully determined. Second, for a reliable InSAR measurement, a network of dense SBAS interferometric pairs needs to be constructed. Besides, the phase unwrapping error needs to be checked carefully, because such an error would become significant on the data margin for phase unwrapping on the network of irregular PTs.

It is worth remarking that not all coastal zones present subsidence signals in the ENVISAT InSAR measurements. It can be explained by temporal decorrelation [25,47], causing few usable PTs to be available. For example, there are several parts in our study area which tend to decorrelate due to a construction process. Compared with the long revisit cycle (35 days) of ENVISAT, the new generation of SAR platforms have shorter revisits, such as the ALOS-2 (14 days) and Sentinel-1A (12 days). SAR images from these new platforms generally maintain much higher coherence. In addition, only

vertical displacement is retrieved, based on the assumption of non-horizontal displacement in this study. However the horizontal displacement cannot be neglected, especially for areas with a large subsidence rate. So combined multiple-pass InSAR datasets with different viewing angles can be considered to reveal ground 3-D deformations further.

6. Conclusions

To meet the demand of urbanization and economic development, about 80 km^2 of land has been reclaimed from the sea in Shenzhen over the past three decades. The reclaimed land undergoes local heterogeneous deformation that affects the stability of both ground constructions and underground man-made facilities. In order to monitor the reclaimed land deformation, we proposed a PTs-based SBAS-InSAR method, which has the ability to detect large amplitude deformation and choose high PTs density in a low coherence area. The spatial and temporal variability of the deformation was discussed over the lands reclaimed over the past decades in Shenzhen. Inter-comparison of the InSAR measurements from different orbits showed that the correlation between these measurements is 0.92, and the RMSE of the difference between these measurements is 1.8 mm/year, implying a good self-consistency of the InSAR measurements. The InSAR measurements showed that the reclaimed land underwent remarkable deformation (up to 25 mm/year in the LOS direction), especially at the Shenzhen Airport, Bao'an Center, Qianhai Bay, and Shenzhen Bay, and the deformation is expected to continue in the near future. Therefore, continuous deformation monitoring is necessary in these reclaimed area.

Acknowledgments: This work is supported by Shenghua Yuying fund of Central South University and the National Natural Science Foundation of China (41474007 and 41404013) and the Fundamental Research Funds of Central South University (2014zzts049). The Landsat images are provided by USGS. General Mapping Tools (v5.1.2) and Gnuplot (v4.4) are exploited to produce several Figures. The authors would like to thank the four anonymous reviewers for their constructive remarks and suggestions.

Author Contributions: Bing Xu, Guangcai Feng and Zhiwei Li conceive the research work, and Bing Xu wrote the first draft of the paper. Guangcai Feng, Zhiwei Li, Qijie Wang, Changcheng Wang, Rongan Xie contributed to experiment implementation and result interpretation. All authors contributed to paper writing and revision.

Conflicts of Interest: The authors declare no conflict of interest.

Abbreviations

The following abbreviations are used in this manuscript:

ASAR	Advanced Synthetic Aperture Radar
DA	Dispersion of Amplitude
DEM	Digital Elevation Model
DS	Distributed Scatterers
ENVISAT	Environmental Satellite
GPS	Global Positioning System
InSAR	Synthetic Aperture Radar Interferometry
LOS	Line-Of-Sight
Land Reclamation	The process of creating new land from ocean, riverbeds, or lake beds.
MT-InSAR	Multi-Temporal InSAR
No.	Number
PS-InSAR	Persistent Scatterer InSAR
PT	Point Target
SBAS	Small Baseline Subset
SBAS-InSAR	Small Baseline Subset InSAR
SLC	Single Look Complex
SNR	Signal-to-Noise Ratio
SRTM	Shuttle Radar Topography Mission
TS	Time Series
3-D	Three-Dimensional

Appendix A

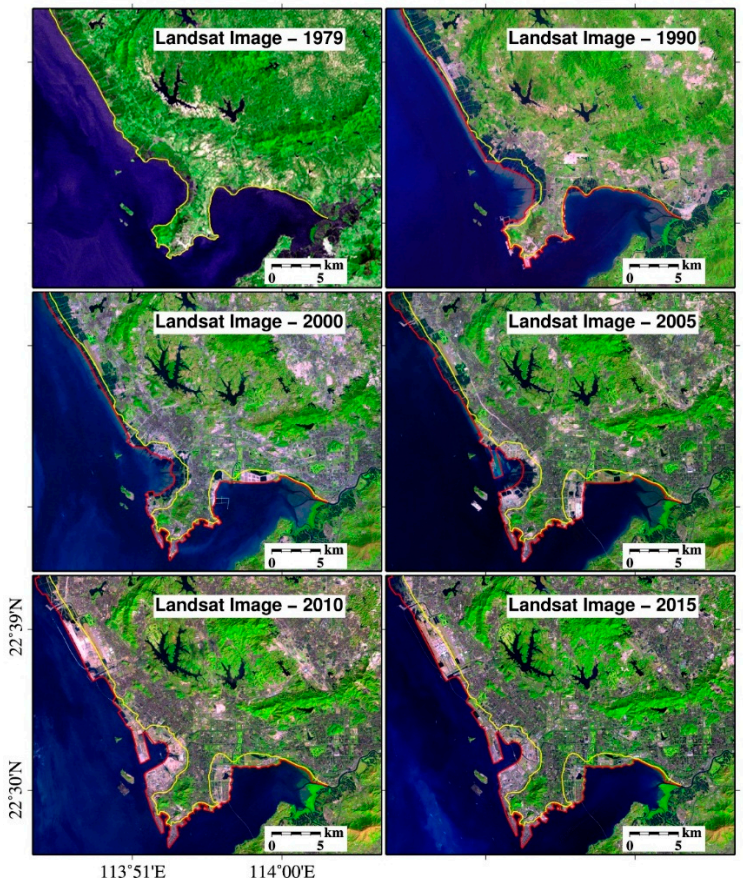

Figure A1. Land reclamation in Shenzhen recorded by the Landsat images. The gray color denotes the urban areas, green represents natural vegetation, and blue represents water. The yellow line is the coastline in 1979. The red line denotes the coastline of the corresponding years.

Table A1. Image datasets of track 025 (ascending).

No.	Acquisition Date	Orbit Number	Perpendicular Baseline (m)	Temporal Baseline (day)	Doppler Baseline (Hz)
1	28 February 2007	26131	1.200	−700	25.565
2	4 April 2007	26632	−44.517	−665	−95.094
3	9 May 2007	27133	53.848	−630	24.165
4	13 June 2007	27634	83.181	−595	−35.858
5	18 July 2007	28135	249.955	−560	−13.692
6	22 August 2007	28636	330.813	−525	−36.740
7	31 October 2007	29638	168.819	−455	10.479
8	5 December 2007	30139	−198.362	−420	10.734
9	9 January 2008	30640	248.996	−385	−19.445
10	19 March 2008	31642	255.402	−315	22.999
11	23 April 2008	32143	141.737	−280	8.279
12	2 July 2008	33145	−93.116	−210	−109.998
13	6 August 2008	33646	216.613	−175	23.050
14	15 October 2008	34648	45.448	−105	20.116
15	19 November 2008	35149	−180.867	−70	−93.809
16	28 January 2009	36151	0.000	0	0.000
17	4 March 2009	36652	67.309	35	27.292
18	8 April 2009	37153	−218.997	70	−72.524
19	13 May 2009	37654	−7.443	105	7.185
20	17 June. 2009	38155	−199.092	140	5.291

Table A1. *Cont.*

No.	Acquisition Date	Orbit Number	Perpendicular Baseline (m)	Temporal Baseline (day)	Doppler Baseline (Hz)
21	22 July 2009	38656	121.769	175	67.987
22	26 August 2009	39157	274.131	210	−1.431
23	30 September 2009	39658	−279.599	245	−92.997
24	13 January 2010	41161	42.797	350	3.044
25	17 February 2010	41662	−116.154	385	−77.225
26	24 March 2010	42163	167.457	420	7.420
27	28 April 2010	42664	−17.800	455	−89.608
28	2 June 2010	43165	201.274	490	20.132
29	7 July 2010	43666	−183.277	525	−36.164
30	11 August 2010	44167	153.339	560	8.991
31	15 September 2010	44668	311.510	595	−0.209

Table A2. Image datasets of track 175 (descending).

No.	Acquisition Date	Orbit Number	Perpendicular Baseline (m)	Temporal Baseline (day)	Doppler Baseline (Hz)
1	24 June 2007	27784	−54.492	−420	−9.713
2	29 July 2007	28285	−120.473	−385	−6.183
3	2 September 2007	28786	64.293	−350	−10.988
4	7 October2007	29287	−177.061	−315	−3.644
5	11 November 2007	29788	87.049	−280	−11.855
6	16 December 2007	30289	−204.988	−245	−9.418
7	20 January 2008	30790	−212.565	−210	−12.067
8	24 February. 2008	31291	−282.373	−175	−6.489
9	30 March 2008	31792	137.053	−140	−7.713
10	4 May 2008	32293	−85.548	−105	−14.254
11	8 June 2008	32794	66.104	−70	−8.627
12	13 July 2008	33295	174.508	−35	−3.449
13	17 August. 2008	33796	0.000	0	0.000
14	21 September 2008	34297	−184.108	35	2.401
15	4 January 2009	35800	36.880	140	−7.600
16	8 February 2009	36301	−227.607	175	−7.695
17	15 March 2009	36802	395.745	210	−2.732
18	19 April 2009	37303	−159.084	245	−16.068
19	24 May 2009	37804	21.721	280	−17.713
20	28 June 2009	38305	156.203	315	−9.648
21	2 August 2009	38806	−116.555	350	−9.147
22	6 September 2009	39307	133.858	385	−8.236
23	20 December 2009	40810	−153.050	490	−11.066
24	28 February 2010	41812	−269.032	560	−1.572
25	4 April 2010	42313	232.788	595	−21.591
26	9 May 2010	42814	171.201	630	−35.714
27	13 June 2010	43315	143.627	665	−15.045
28	22 August 2010	44317	−191.774	735	−7.937

Table A3. Statistics of the phase unwrapping error in track 025.

Phase Unwrapping Error (rad)	Qianhai Bay	Shenzhen Bay	Whole Area
	Percentage (%)	Percentage (%)	Percentage (%)
[−0.5, 0.5]	82.70	83.33	85.12
[−1.0, 1.0]	95.35	96.06	96.53
[−1.5, 1.5]	98.98	99.14	99.26

Table A4. Statistics of the phase unwrapping error in track 175.

Phase Unwrapping Error (rad)	Qianhai Bay	Shenzhen Bay	Whole Area
	Percentage (%)	Percentage (%)	Percentage (%)
[−0.5, 0.5]	82.81	86.43	87.15
[−1.0, 1.0]	96.25	97.52	97.65
[−1.5, 1.5]	99.46	99.58	99.63

Appendix B

To evaluate the effectiveness of the proposed strategy, the dataset from track 175 is processed with the STAMPS PSI method [21,49] (see Figure B1). Numerous PTs in built-up areas have been detected by the STAMPS method and the proposed method. However, in low-coherence areas, the STAMPS method can select few PTs due to the decorrelation effect, while our strategy can select an appropriate number of PTs. The density of PTs selected by STAMPS is 301 points/km^2, however, it is 779 points/km^2 by our method. Such difference is particularly evident in reclaimed land areas, such as Bao'an Center, the north to the Shenzhen Bay Checkpoint, and the dam of Shenzhen Airport.

For more detailed comparison, the regions A and B marked with a black rectangle (see Figure B1) were further analyzed with zoom-in view shown in Figures B2 and B3. The deformation rate maps obtained by STAMPS and our method have a very similar deformation trend (see Figures B2 and B3). However, our deformation rate can detect much larger deformation than that of the STAMPS results. As shown in Figures B2 and B3, few PTs have been selected from areas with large deformations by the STAMPS method. As a consequence, the area that undergoes rapid deformation has few measurements on STAMPS results, while appropriate PTs have been identified by our method for deformation mapping.

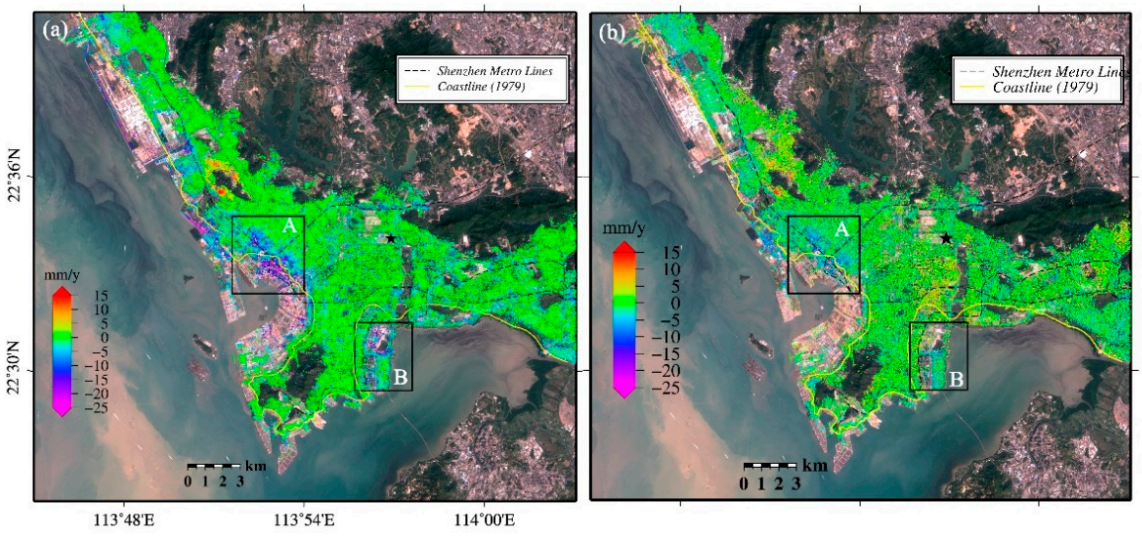

Figure B1. Deformation rate maps extracted by (**a**) PT-based SBAS-InSAR and (**b**) STAMPS. We can see that more PTs have been selected by our method (PT-based SBAS-InSAR). Regions A and B are further analyzed.

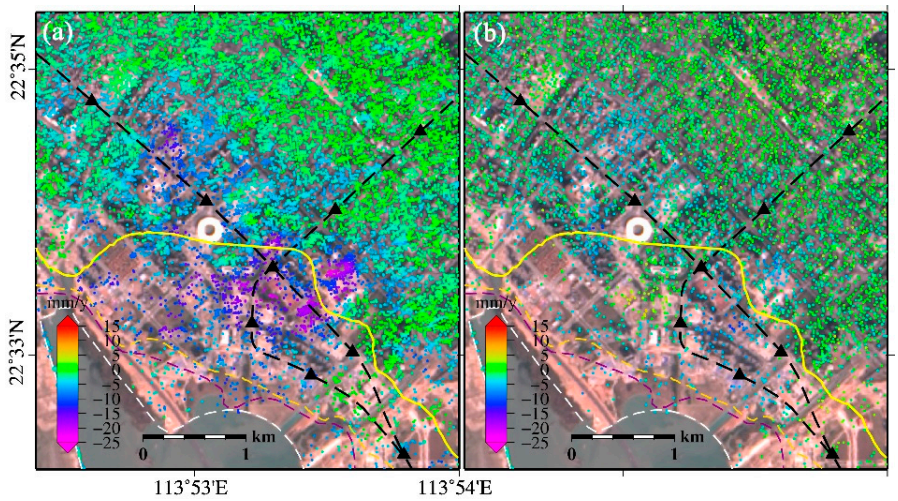

Figure B2. Deformation rate maps for region A, Bao'an Center extracted by (**a**) PT-based SBAS-InSAR and (**b**) STAMPS. Numerous PTs have been selected in the urban area, upper-right part of the Figure. However, the density of PTs selected by our method is larger than that of STAMPS, especially in areas with large deformation. However, in (**b**) the significant deformation could not be well mapped, due to the sparse PTs density of the STAMPS method.

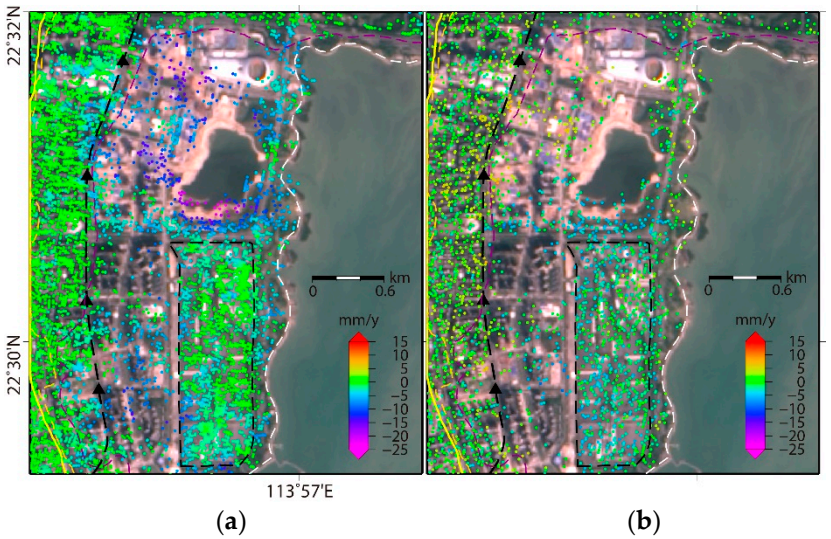

Figure B3. Deformation rate maps for region B, Shenzhen Bay extracted by (**a**) PT-based SBAS-InSAR and (**b**) STAMPS. Numerous PTs have been selected in the urban area. However, our method can select more PTs than the STAMPS method in areas with a large deformation rate, especially the northern part of the Shenzhen Bay Check Point, which enables us to map the significant deformation.

References

1. Shi, Y. Exacerbating coastal hazards and defensive countermeasures in China. *J. Nat. Disasters* **1994**, *3*, 3–15.
2. Zhu, X. Remote sensing monitoring of coastline change in Pearl River Estuary. In Proceedings of the 22nd Asian Conference on Remote Sensing, Singapore, 5–9 November 2001.
3. Wali, M.K. *Practices and Problems of Land Reclamation in Western North America*; University of North Dakota Press: Grand Forks, ND, USA, 1975.
4. Suzuki, T. Economic and geographic backgrounds of land reclamation in Japanese ports. *Mar. Pollut. Bull.* **2003**, *47*, 226–229. [CrossRef]

5. Breber, P.; Povilanskas, R.; Armaitienė, A. Recent evolution of fishery and land reclamation in curonian and lesina lagoons. *Hydrobiologia* **2008**, *611*, 105–114. [CrossRef]
6. Hoeksema, R.J. Three stages in the history of land reclamation in the Netherlands. *Irrig. Drain.* **2007**. [CrossRef]
7. De Mulder, E.; Van Bruchem, A.; Claessen, F.; Hannink, G.; Hulsbergen, J.; Satijn, H. Environmental impact assessment on land reclamation projects in the Netherlands: A case history. *Eng. Geol.* **1994**, *37*, 15–23. [CrossRef]
8. Bi, X.; Liu, F.; Pan, X. Coastal projects in China: From reclamation to restoration. *Environ. Sci. Technol.* **2012**, *46*, 4691–4692. [CrossRef] [PubMed]
9. Gao, G.D.; Wang, X.H.; Bao, X.W. Land reclamation and its impact on tidal dynamics in Jiaozhou Bay, Qingdao, China. *Estuarine Coast. Shelf Sci.* **2014**, *151*, 285–294. [CrossRef]
10. Wang, W.; Liu, H.; Li, Y.; Su, J. Development and management of land reclamation in China. *Ocean Coast. Manag.* **2014**, *102*, 415–425. [CrossRef]
11. Rosen, P.A.; Hensley, S.; Joughin, I.R.; Li, F.K.; Madsen, S.N.; Rodriguez, E.; Goldstein, R.M. Synthetic aperture radar interferometry. *Proc. IEEE* **2000**, *88*, 333–382. [CrossRef]
12. Bamler, R.; Hartl, P. Synthetic aperture radar interferometry. *Inverse. Prob.* **1998**, *14*, R1–R54. [CrossRef]
13. Feng, G.C.; Li, Z.W.; Xu, B.; Shan, X.J.; Zhang, L.; Zhu, J.J. Coseismic deformation of the 2015 MW 6.4 Pishan, China, earthquake, estimated from Sentinel1 and ALOS2 data. *Seismol. Res. Lett.* **2016**. [CrossRef]
14. Feng, G.C.; Li, Z.W.; Shan, X.J. Geodetic model of the April 25, 2015 MW 7.8 Gorkha Nepal earthquake and MW 7.3 aftershock estimated from InSAR and GPS data. *Geophys. J. Int.* **2015**, *203*, 896–900. [CrossRef]
15. Feng, G.; Li, Z.; Shan, X.; Xu, B.; Du, Y. Source parameters of the 2014 mw 6.1 south Napa earthquake estimated from the Sentinel 1a, Cosmo-skymed and GPS data. *Tectonophysics* **2015**, *605*, 139–146.
16. Lu, Z.; Dzurisin, D.; Biggs, J.; Wicks, C.; McNutt, S. Ground surface deformation patterns, magma supply, and magma storage at Okmok volcano, Alaska, from InSAR analysis: 1. Intereruption deformation, 1997–2008. *J. Geophys. Res. Solid Earth* **2010**. [CrossRef]
17. Lu, Z.; Masterlark, T.; Dzurisin, D. Interferometric synthetic aperture radar study of Okmok volcano, Alaska, 1992–2003: Magma supply dynamics and postemplacement lava flow deformation. *J. Geophys. Res. Solid Earth* **2005**. [CrossRef]
18. Berardino, P.; Fornaro, G.; Lanari, R.; Sansosti, E. A new algorithm for surface deformation monitoring based on small baseline differential SAR interferograms. *IEEE Trans. Geosci. Remote Sens.* **2002**, *40*, 2375–2383. [CrossRef]
19. Lanari, R.; Mora, O.; Manunta, M.; Mallorquí, J.J.; Berardino, P.; Sansosti, E. A small-baseline approach for investigating deformations on full-resolution differential SAR interferograms. *IEEE Trans. Geosci. Remote Sens.* **2004**, *42*, 1377–1386. [CrossRef]
20. Ferretti, A.; Prati, C.; Rocca, F. Permanent scatterers in SAR interferometry. *IEEE Trans. Geosci. Remote Sens.* **2001**, *39*, 8–20. [CrossRef]
21. Hooper, A. A multi-temporal INSAR method incorporating both persistent scatterer and small baseline approaches. *Geophys. Res. Lett.* **2008**. [CrossRef]
22. Zhang, R.; Liu, G.; Li, Z.; Zhang, G.; Lin, H.; Yu, B.; Wang, X. A hierarchical approach to persistent scatterer network construction and deformation time series estimation. *Remote Sens.* **2015**, *7*, 211. [CrossRef]
23. Solari, L.; Ciampalini, A.; Raspini, F.; Bianchini, S.; Moretti, S. PsInSAR analysis in the pisa urban area (Italy): A case study of subsidence related to stratigraphical factors and urbanization. *Remote Sens.* **2016**, *8*, 120. [CrossRef]
24. Li, Z.W.; Zhao, R.; Hu, J.; Wen, L.X.; Feng, G.C.; Zhang, Z.Y.; Wang, Q.J. InSAR analysis of surface deformation over permafrost to estimate active layer thickness based on one-dimensional heat transfer model of soils. *Sci. Rep.* **2015**. [CrossRef] [PubMed]
25. Zebker, H.A.; Villasenor, J. Decorrelation in interferometric radar echoes. *IEEE Trans. Geosci. Remote Sens.* **1992**, *30*, 950–959. [CrossRef]
26. Li, Z.; Xu, W.; Feng, G.; Hu, J.; Wang, C.; Ding, X.; Zhu, J. Correcting atmospheric effects on InSAR with meris water vapour data and elevation-dependent interpolation model. *Geophys. J. Int.* **2012**, *189*, 898–910. [CrossRef]
27. Li, Z.; Ding, X.; Huang, C.; Zou, Z.; Chen, Y. Atmospheric effects on repeat-pass InSAR measurements over Shanghai region. *J. Atmos. Sol. Terr. Phys.* **2007**, *69*, 1344–1356. [CrossRef]

28. Li, Z.; Fielding, E.; Cross, P.; Preusker, R. Advanced InSAR atmospheric correction: MERIS/MODIS combination and stacked water vapour models. *Int. J. Remote Sens.* **2009**, *30*, 3343–3363. [CrossRef]
29. Li, Z.; Fielding, E.; Cross, P. Integration of INSAR time-series analysis and water-vapor correction for mapping postseismic motion after the 2003 BAM (Iran) earthquake. *IEEE Geosci. Remote Sens. Lett.* **2009**, *47*, 3220–3230.
30. Jiang, L.; Lin, H. Integrated analysis of SAR interferometric and geological data for investigating long-term reclamation settlement of Chek Lap Kok Airport, Hong Kong. *Eng. Geol.* **2010**, *110*, 77–92. [CrossRef]
31. Cianflone, G.; Tolomei, C.; Brunori, C.; Dominici, R. InSAR time series analysis of natural and anthropogenic coastal plain subsidence: The case of Sibari (Southern Italy). *Remote Sens.* **2015**, *7*, 15812. [CrossRef]
32. Teatini, P.; Tosi, L.; Strozzi, T.; Carbognin, L.; Wegmuller, U.; Rizzetto, F. Mapping regional land displacements in the venice coastland by an integrated monitoring system. *Remote Sens. Environ.* **2005**, *98*, 403–413. [CrossRef]
33. Pfeffer, J.; Allemand, P. The key role of vertical land motions in coastal sea level variations: A global synthesis of multisatellite altimetry, tide gauge data and GPS measurements. *Earth Planet. Sci. Lett.* **2016**, *439*, 39–47. [CrossRef]
34. Han, X.; Long, J.; Li, J.; Chu, F.; Zhang, P.; Xu, D.; Yang, H. Research progress on the vulnerability of the Pearl River Delta. *Trop. Geogr.* **2010**, *1*, 002.
35. Zhang, H.M.; Xu, Y.S.; Zeng, Q.L. Deformation behavior of shenzhen soft clay and post-construction settlement. *Chin. J. Geotech. Eng.* **2002**, *24*, 509–514. (In Chinese with English Abstract)
36. Wang, H.; Wright, T.J.; Yu, Y.; Lin, H.; Jiang, L.; Li, C.; Qiu, G. InSAR reveals coastal subsidence in the Pearl River Delta, China. *Geophys. J. Int.* **2012**, *191*, 1119–1128. [CrossRef]
37. Li, Y.; Wang, Y.; Peng, J.; Liu, Z.; Wu, J. Assessment of loss of ecosystem service value under sea-level rise: A case study of Shekou Peninsula in Shenzhen. *Prog. Geogr.* **2009**, *28*, 417–423.
38. Ferretti, A.; Fumagalli, A.; Novali, F.; Prati, C.; Rocca, F.; Rucci, A. A new algorithm for processing interferometric data-stacks: SQUEESAR. *IEEE Trans. Geosci. Remote Sens.* **2011**, *49*, 3460–3470. [CrossRef]
39. Zhou, H.; Hu, J.; Liu, X.; Ren, P. Ground deformation monitoring of shenzhen metro area with interferometric point target analysis. In Proceedings of the IEEE 2012 20th International Conference on Geoinformatics, Hong Kong, 15–17 June 2012; pp. 1–5.
40. Du, W. *Reaseach on the Regulation of Soft Clay Foundation in Shenzhen*; China University of Geosciences: Wuhan, China, 2007.
41. Chen, W.-G.; Zhao, H.-M.; Li, F.-G. Fault activities and their influence upon geologic environment in Shenzhen city. *Trop. Geogr.* **2001**, *21*, 45–60.
42. Jia, J.; Sun, J.; Zhan, W.; Yi, S. The current situation and problem of geological environment in Shenzhen city. *J. Eng. Geol.* **2006**, *14*, 33–37.
43. Yeh, A.G.O.; Li, X. An integrated remote sensing and GIS approach in the monitoring and evaluation of rapid urban growth for sustainable development in the Pearl River Delta, China. *Int. Plan. Stud.* **1997**, *2*, 193–210. [CrossRef]
44. Seto, K.C.; Woodcock, C.; Song, C.; Huang, X.; Lu, J.; Kaufmann, R. Monitoring land-use change in the Pearl River Delta using Landsat TM. *Int. J. Remote Sens.* **2002**, *23*, 1985–2004. [CrossRef]
45. Li, X.; Damen, M.C. Coastline change detection with satellite remote sensing for environmental management of the Pearl River Estuary, China. *J. Mar. Syst.* **2010**, *82*, S54–S61. [CrossRef]
46. Shenzhen Bureau of Statistics. *Statistical Review of Shenzhen, 2007*; China Statistics Press: Beijing, China, 2007; Volume 17, pp. 107–124.
47. Jiang, M.; Ding, X.; Li, Z.; Tian, X.; Wang, C.; Zhu, W. InSAR coherence estimation for small data sets and its impact on temporal decorrelation extraction. *IEEE Trans. Geosci. Remote Sens.* **2014**, *52*, 6584–6596. [CrossRef]
48. Werner, C.; Wegmüller, U.; Strozzi, T.; Wiesmann, A. Gamma SAR and interferometric processing software. In Proceedings of the ERS-ENVISAT Symposium, Gothenburg, Sweden, 16–20 October 2000.
49. Hooper, A.J. Persistent Scatter Radar Interferometry for Crustal Deformation Studies and Modeling of Volcanic Deformation. Ph.D. Thesis, Stanford University, Stanford, CA, USA, 2006.
50. Rabus, B.; Eineder, M.; Roth, A.; Bamler, R. The shuttle radar topography mission—A new class of digital elevation models acquired by spaceborne radar. *ISPRS J. Photogramm. Remote Sens.* **2003**, *57*, 241–262. [CrossRef]

51. Jiang, M.; Ding, X.; Li, Z. Hybrid approach for unbiased coherence estimation for multitemporal InSAR. *IEEE Trans. Geosci. Remote Sens.* **2014**, *52*, 2459–2473. [CrossRef]
52. Werner, C.; Wegmüller, U.; Strozzi, T.; Wiesmann, A. Interferometric point target analysis for deformation mapping. In Proceedings of the Geoscience and Remote Sensing Symposium, Toulouse, France, 21–25 July 2003; pp. 4362–4364.
53. Smith, S.M.; Brady, J.M. SUSAN—A new approach to low level image processing. *Int. J. Comput. Vision* **1997**, *23*, 45–78. [CrossRef]
54. Xu, B.; Yin, H.; Zhu, J.; Wang, C. InSAR interferogram filtering based on SUSAN and its improved algorithm. *J Geod. Geodyn.* **2010**, *30*, 68–73.
55. Costantini, M. A novel phase unwrapping method based on network programming. *IEEE Trans. Geosci. Remote Sens.* **1998**, *36*, 813–821. [CrossRef]
56. Doornbos, E.; Scharroo, R. Improved ERS and Envisat precise orbit determination. In Proceedings of the Envisat & ERS Symposium, Salzburg, Austria, September 2004; pp. 6–10.
57. Xu, B.; Li, Z.-W.; Wang, Q.-J.; Jiang, M.; Zhu, J.-J.; Ding, X.-L. A refined strategy for removing composite errors of SAR interferogram. *IEEE Geosci. Remote Sens. Lett.* **2014**, *11*, 143–147. [CrossRef]
58. Plant, G.W.; Covil, C.S.; Hughes, R.A. *Site Preparation for the New Hong Kong International Airport—The Design, Construction and Performance of the Airport Platform*; Thomas Telford: London, UK, 1998.
59. Gernhardt, S. High Precision 3D Localization and Motion Analysis of Persistent Scatterers Using Meter-Resolution Radar Satellite Data. Ph.D. Thesis, Technische Universität München, München, Germany, 2011.
60. Ge, L.; Ng, A.H.M.; Li, X.; Abidin, H.Z.; Gumilar, I. Land subsidence characteristics of Bandung Basin as revealed by envisat ASAR and ALOS PALSAR interferometry. *Remote Sens. Environ.* **2014**, *154*, 46–60. [CrossRef]
61. Porter, T.; Duff, T. Compositing digital images. In *ACM SIGGRAPH Computer Graphics*; ACM: New York, NY, USA, 1984; pp. 253–259.
62. Le Cozannet, G.; Raucoules, D.; Wöppelmann, G.; Garcin, M.; Da Sylva, S.; Meyssignac, B.; Gravelle, M.; Lavigne, F. Vertical ground motion and historical sea-level records in Dakar (Senegal). *Environ. Res. Lett.* **2015**, *10*, 084016. [CrossRef]
63. Yin, J.-P.; Xie, Q.; Sun, Z.-X.; Chen, J. Status of seawater intrusion into coastal area of Shenzhen. *Mar. Environ. Sci.* **2011**, *30*, 541–545.
64. Huang, Z.; Zong, Y.; Zhang, W. Coastal inundation due to sea level rise in the Pearl River Delta, China. *Nat. Hazard.* **2004**, *33*, 247–264. [CrossRef]
65. Church, J.A.; White, N.J. Sea-level rise from the late 19th to the early 21st century. *Surv. Geophys.* **2011**, *32*, 585–602. [CrossRef]
66. Klein, R.J.T.; Nicholls, R.J.; Sachooda, R.; Michele, C.; James, A.; Buckley, E.N. Technological options for adaptation to climate change in coastal zones. *J. Coast. Res.* **2001**, *17*, 531–543.